J. Fluid Mech. (2000), *vol.* 422, *pp.* 55–68. Printed in the United Kingdom

Highly turbulent Couette–Taylor bubbly flow patterns

By K. ATKHEN[1], J. FONTAINE[1]† AND J. E. WESFREID[2]

[1]CEA Valrhô, DRRV/SEMP/LGC, BP 171, F-30207 Bagnols-sur-Cèze, France
[2]ESPCI/PMMH (UA 857 CNRS), 10 rue Vauquelin, F-75231 Paris Cedex 05, France

(Received 12 December 1997 and in revised form 19 May 2000)

We present the results of experimental study of a Couette–Taylor system with superimposed axial flow and an upper free surface, in the high Taylor number regime. At large Taylor numbers, when the rotational speed of the inner cylinder increases, bubbles created near the free surface are distributed throughout the test section and permit the study of the spatial and temporal properties of turbulent flows using visualization techniques. In addition to classic travelling Taylor vortices, intermittent pulses of vortices with higher phase velocities are also observed. These patterns are described in terms of the rotational speed and the intensity of the throughflow.

1. Introduction

Couette–Taylor instabilities are prototypes for general studies in hydrodynamic stability and transition to turbulence. Less known are various industrial applications of these characteristic patterns coupled with an axial flow, such as cooling of rotating machinery or in continuous chemical reactors. Each pair of vortices can be idealized, in a first approximation, as a well-mixed batch reactor advected by the axial flow and without exchange of liquid between the adjacent vortices (figure 1*a*). This property can be useful in liquid–liquid contact devices used in nuclear fuel reprocessing because it may allow accurate control of the fluid residence time.

In the nuclear fuel cycle, the main steps of the reprocessing are carried out by liquid extraction cycles (Treybal 1981). Liquid extraction is the separation of the constituents of an aqueous solution by contact with another insoluble organic liquid. The purpose of the equipment used for the liquid–liquid operations is to provide intimate contact between the two fluids for a sufficient time to permit interphase mass transfer of the energetic elements (uranium and plutonium). The rate of mass transfer is directly dependent upon the interface surface area between the phases. Intense agitation is thus required to generate an emulsion composed of small droplets (with a diameter smaller than 500 μm), and consequently to increase the rate of mass transfer; this involves flows characterized by very high Taylor number, Ta. Moreover, the typical flow rates in a reprocessing plant induce a significant axial flow in such liquid extraction devices, which implies a relatively high axial Reynolds number, Re. Such innovative applications to chemical and nuclear engineering follow up original fundamental problems related to the Couette–Taylor instability for multi-phase flows and highly turbulent situations.

† Present address: CEA Valrhô, DTE, B.P. 111, F-26702 Pierrelatte, France.

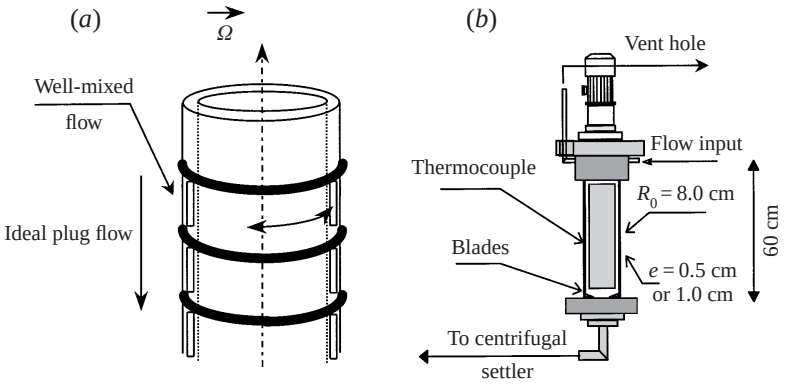

FIGURE 1. (*a*) Ideal flow configuration from a chemical engineering standpoint: each vortex is considered as a well-mixed reactor axially advected in such a way that the flow can globally be modelled by an ideal plug flow. (*b*) Sketch of the prototype.

In the last 30 years, a substantial amount of research has been conducted on various aspects of Couette–Taylor flows. Recently, there has been increasing interest in turbulent situations (Marcus 1984; Lathrop, Fineberg & Swinney 1992, for example).

In the case of a circular Couette flow with superimposed axial throughput, the flow patterns are expected to be more complicated due to strong interactions between axial and rotating flows. In 1990, Bühler & Polifke presented theoretical and experimental results on the stability and time behaviour of such a case. Concerning mass transfer in such flows, Ohmura *et al.* (1997), after Tam & Swinney (1987), focused their attention on exchanges between the cell boundaries in the weakly turbulent wavy vortex flow. They found an intercell mixing coefficient depending on the Taylor number but also on the axial wavelength.

Recently, Wereley & Lueptow (1999) analysed the velocity field of axially moving Taylor vortex flow using the Particle Image Velocimetry (PIV) technique, and showed that for low values of the Ta/Re ratio the exchange of fluid between vortices is relatively important and vice versa. Moreover, like Snyder (1962), Lueptow, Docter & Min (1992) and Piva *et al.* (1997), these authors noticed that the phase velocity of the vortices is greater than the average axial velocity.

Kataoka & Takigawa (1981) investigated the mixing properties of higher turbulent flows, and showed that the toroidal motion of fluid elements causes highly effective radial mixing within cellular vortices, whereas the cell boundaries act like barriers to mass exchanges. In addition, Kataoka, Doi & Hongo (1975) reported a possible practical application of the axially moving Taylor vortex flow to a liquid–liquid surface reaction in the range of $0 < Re < 20$ and $246 < Ta < 500$.

However, as mentioned above, the working constraints in a reprocessing plant lead to operation in a region of the Taylor/Reynolds numbers map that has been rarely explored in previous work. Moreover, in the presence of an upper free surface in the gap, when the rotational speed of the inner cylinder increases, bubbles distribute throughout the working cell (Shiomi *et al.* 1993; Djéridi *et al.* 1998). These bubbles become typical tracers and permit the study of the spatial and temporal structures.

In an initial approach to these complex flows, we consider in this paper a single-liquid flow with bubbles. The present study describes the turbulent bubbly flows in a Couette–Taylor–Poiseuille system by means of visualization techniques. The spatial and temporal properties of the vortices are analysed. The results can allow a

better understanding of combined rotating–axial flow in such a device, and provide information for modelling this kind of chemical reactor. We also present results concerning the flow states at previously unexplored (Ta, Re) values.

2. Experimental methods

The experimental prototype reactor is shown schematically in figure 1(*b*). The working cell is composed of a stationary transparent Plexiglas outer cylinder ($R_0 = 8.0\,\text{cm}$) and a rotating stainless steel inner cylinder ($R_{i,1} = 7.5\,\text{cm}$ and $R_{i,2} = 7.0\,\text{cm}$ in a second run of experiments); the concentric annular gap e is thus 0.5 cm (or 1.0 cm) and $\eta = R_{i,1}/R_0 \approx 0.94$ (or $\eta = R_{i,2}/R_0 \approx 0.88$). The test section is 60 cm high (L) but most of the experiments were carried out with a free surface located between 40 and 50 cm from the bottom of the device. Its aspect ratio (L/e) is very large. The upper part of the cell is open to a vent hole. The inner cylinder is rotated by means of an electric motor and an assembly allowing removal from above. This feature is used in nuclear engineering because it permits easy maintenance of the moving parts. Both the motor and the inner cylinder can thus be removed from a highly radioactive zone located beneath a concrete slab and transferred to a maintenance cell.

The rotational speeds of the inner cylinder are $n \in [40\,;2200\,\text{r.p.m.}$ (revolutions per minute)] in the case of $e = 0.5\,\text{cm}$ and $n \in [40\,;3000\,\text{r.p.m.}]$ when $e = 1.0\,\text{cm}$. Water supplied from a vessel is pumped into the device through a pipe at flow rates of $Q \in [0\,;2.5 \times 10^{-4}\,\text{m}^3\,\text{s}^{-1}]$ (0–900 $\text{l}\,\text{h}^{-1}$). As the experimental test-bed pump can ensure high capacity flows but is unsuitable for smaller ones, the $[0\,;300\,\text{l}\,\text{h}^{-1}]$ range is not studied in this paper. Taking into account the effects of the rising temperature, these external conditions correspond, in the case of $e = 0.5\,\text{cm}$, to Taylor number ranges between 40 and 3.5×10^4, and to axial Reynolds numbers between 0 and 560. When $e = 1.0\,\text{cm}$, these numbers vary respectively within the $[40\,;10^5]$ and $[0\,;590]$ ranges. The Taylor and Reynolds numbers are defined as follows:

$$Ta = \left(\frac{e}{R_i}\right)^{1/2} \frac{\Omega R_i e}{\nu}, \qquad Re = \frac{V_m e}{\nu} \quad \text{with} \quad V_m = \frac{Q}{\pi(R_0^2 - R_i^2)},$$

where Ω is the inner-cylinder rotation speed and ν the kinematic viscosity.

In the gap, the liquid is ejected from the pipe and impinges on the inner cylinder. It flows down the rotating wall and reaches the free surface. It then crosses the reactor and is finally ejected from the device through a central hole. However, the rotating surface at the bottom of the inner cylinder induces a strong recirculation current that can hinder the main outflow. Blades were added at the bottom of the static vessel to let the fluid flow out of the reactor; the blades push up the recirculation current and allow the fluid to flow down more easily. The water temperature is measured with a thermocouple inserted in the gap to correct the value of the kinematic viscosity and thus the Taylor and Reynolds numbers. In fact, without a throughflow, we noted a temperature rise due to viscous heating (about 20 °C in 30 minutes at 1500 r.p.m. in the case of $e = 0.5\,\text{cm}$). We also observed that the temperature appeared to be higher at the bottom of the cell. As the inner cylinder rides on a pendular assembly, this indicates that heating of the seals and bearings does not contribute in an appreciable way to the temperature rise.

Two different tracers were used to observe flow patterns, using uniform illumination provided by halogen lamps. For low rotational speeds (figure 2*a*), we added $2\,\text{g}\,\text{l}^{-1}$ of Iriodin® to the water to visualize all the separatrices of the Taylor vortices (Gauthier,

Gondret & Rabaud 1998). Above 500 r.p.m., the agitation of the free surface is sufficiently intense to generate air bubbles that are entrained downward (figure 2*b*) making it possible to study the spatial and temporal properties of the turbulent flows using visualization techniques. In the gap, the bubble size distribution is controlled by the breakage and coalescence phenomena. Two mirrors were set up around the working cell to observe the nature of the patterns in order to analyse the flow configurations in the azimuthal direction.

In view of the high fluid rotation speeds, we use a high-speed linear CCD camera (Lord Ingénierie®, type CNL 2048/Sh) that can acquire a line of 2048 pixels at a maximum frequency of 2000 Hz (figure 2*b*). In practice, the camera sends data resulting from a 3-s exposure to the RAM of a PC; the data are then written to the hard disk. Each pixel is encoded over 8 bits (256 grey levels), and space/time diagrams appear in tabular form to be processed and converted into images. Processing a typical linear camera image generates a 16 MB file.

3. Results

3.1. *Flow configuration*

At low rotation speed (less than 500 r.p.m.), we use Iriodin® particles as tracers. In the first supercritical regimes, we are able to distinguish both inflow and outflow boundaries (figure 2*a*). At higher speeds, only every other boundary is visible, probably the one corresponding to the outer streamlines of the Taylor vortices, close to the rotor.

When the rotational speed reaches 500 r.p.m., air bubbles give a better contrast than Iriodin® for observing the behaviour of the vortices. However, most of the results were drawn from space/time diagrams, using bubbles as tracers (figure 2*b*). Cross-checking the axial wavelength measured using the two different tracers indicates that bubbles are located at every other boundary. Because of their lower density, bubbles are centrifuged inward. In order to explain why the bubble distribution is not uniform along the inner cylinder, however, we must estimate the conditions of stability of the bubble positions on the outflow and inflow separatrices.

The creaming velocity of a bubble, obtained by the equilibrium between buoyancy force and Stokes drag, is

$$V_c = \frac{2r_b^2\tilde{g}(\rho-\rho_b)(\mu+\mu_b)}{3\mu(2\mu+3\mu_b)},$$

where r_b, ρ_b and μ_b are respectively the bubble radius, density and viscosity, and $\tilde{g}$ is the gravity acceleration (Landau & Lifshitz 1987). The velocity fluctuations v_z and v_r are proportional to $(v/e)(Ta-Ta_c)^{1/2}$, where Ta_c is the critical Taylor number of the first instability (Davey, DiPrima & Stuart 1968). If the bubble is located in an equilibrium state along the inner cylinder, at the outflow separatrix, an upward vertical perturbation can be stable if the velocity v_z directed downwards on the separatrix is greater than the upward velocity V_c. The particle thus returns to the original equilibrium position. This occurs for

$$Ta > Ta_c + \left(k\frac{2r_b^2\tilde{g}(\rho-\rho_b)(\mu+\mu_b)}{3\mu(2\mu+3\mu_b)}\frac{e}{v}\right)^2$$

where k is a constant of proportionality. The same calculation can be repeated including the radial velocity fluctuation v_r, and considering $\tilde{g}$ as the centrifugal

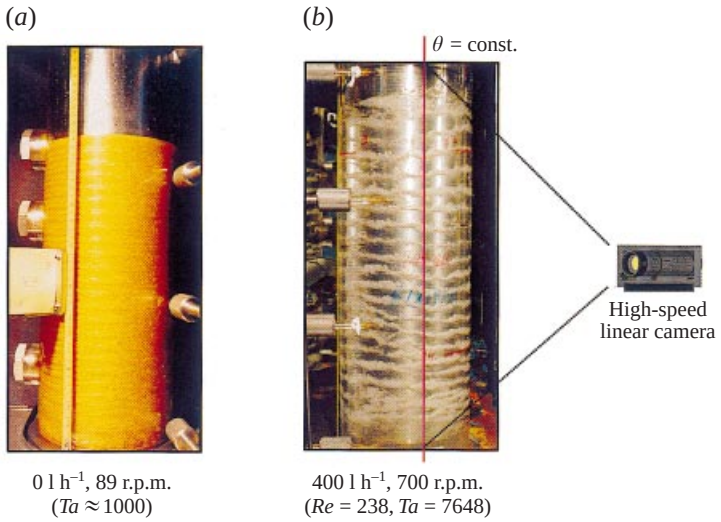

FIGURE 2. (*a*) At low Taylor numbers, using Iriodin® particles as tracers, all the boundaries can be visualized. (*b*) Air bubbles entrained down the length of the cylinder (in both cases $e = 0.5$ cm).

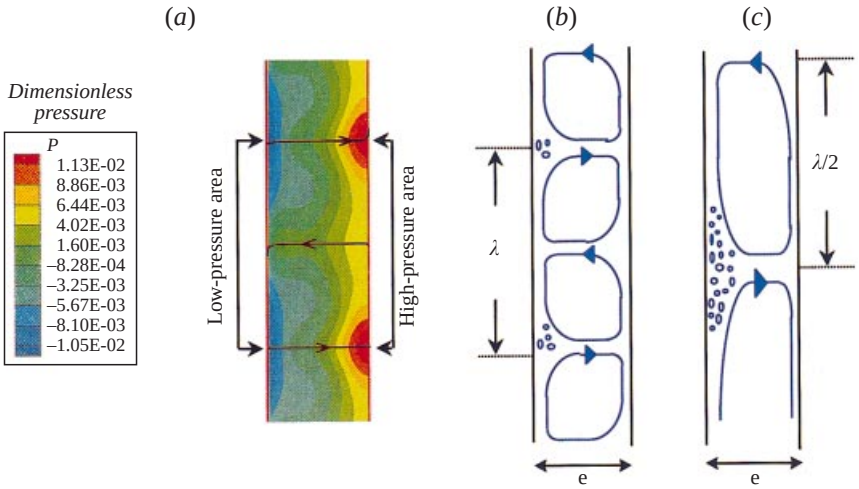

FIGURE 3. (*a*) Pressure field ($Ta = 152$ and $L/e = 12$) computed with a direct numerical simulation code based on spectral element methods (Magère *et al.* 1998); minima are located near the outflow against the rotor. (*b*) Low rotational speed: air bubbles accumulate at every other boundary (outflows). (*c*) High rotational speed: bubbles accumulate against the rotor along the outflow.

acceleration. Using the same approach, it can be shown that a bubble located on the inflow separatrix is not in the equilibrium state. For sufficiently high Taylor number values, the preferred bubble position is on the outflow separatrix, along the inner cylinder.

The conditions of stability of a bubble near the centre of a roll were analysed by Djéridi *et al.* (1998) and Favé (1999). They showed by the force balance on a bubble (drag force, buoyancy force, centrifugal force induced by the Couette flow and inertial force directed to the centre of the Taylor rolls) that the position near the centre of the rolls is stable only at low Taylor numbers. This analysis is consistent with our results:

at low Taylor numbers, the bubbles are captured alternately below and above the centre, showing the alternance of wide and narrow spacing of observed bubble rings (see next paragraph). As the Taylor number increases, the bubbles migrate towards the inner cylinder at the outflow regions as discussed above. The ring spacing is thus identified with the axial wavelength. Moreover, for lower Ta, a direct numerical simulation of the single-phase Couette–Taylor flow using a spectral element method (Magère *et al.* 1998) also shows that the pressure field is minimal along the outflow against the rotor (figure 3*a*, $Ta = 152$ and $L/e = 12$). Because of their lower density, air bubbles can remain there and accumulate as the rotational speed increases (figures 3*b* and 3*c*). In any event, bubble lines accurately represent the vortex patterns when the influence of the buoyancy force is offset by the effects of the rotational speed, allowing the bubbles to be trapped in the flow.

When the Ta/Re ratio is relatively low, the parallel ring configuration cannot remain steady, because of merging and splitting phenomena. Such phenomena, which are well known for Dean rolls, another centrifugal instability (Ligrani *et al.* 1994), have not previously been reported for Taylor rolls. Most of the structures detected are spirals with many spatial and temporal defects (figure 4*a*). As the rotational speed increases, centrifugal effects prevail and air bubbles become organized into parallel rings advected by the axial throughflow (figure 4*b*). No significant inclination angle of the Taylor vortices has been noted. This flow configuration seems to be ideal from a chemical engineering standpoint because it allows for accurate control of the residence time in the reactor (figure 1*a*).

Further increasing the rotational speed implies increasing agitation of the top free surface. Thus, spatial and temporal defects gradually invade the entire cylinder from the top free surface, finally leading to the destruction of the vortices. On the other hand, the influence of the entry length of the perturbation due to the lower boundary condition (blades) remains constant whatever operational conditions (figures 4*c* and 4*d*). In figure 4(*d*), note the characteristic size of the pattern inhomogeneity, which varies with both the Taylor and Reynolds numbers. As a consequence of this perturbation, the boundaries of the Taylor vortices oscillate, resulting in overlapping and intermixing between adjacent cells. The cell structures progressively degenerate to a disorderly pattern. Merging and splitting phenomena dominate the whole annulus so that the vortices cannot be easily detected (figure 4*c*). This flow configuration is observed beyond $Ta > 2 \times 10^4$ in the case of $e = 0.5\,\text{cm}$ and $Ta > 5 \times 10^4$ when $e = 1.0\,\text{cm}$.

We also found anomalous flow configurations, revealed by high-speed linear camera exposures. They do not dominate the flow in time and are not present in every experimental run. One of these 'non-trivial configurations' involves very large intermittent pulses of vortices travelling with high velocities. For example, when $Ta = 6940$ and $Re = 216$ ($e = 0.5\,\text{cm}$), we can observe these particular flows where the vortices descend rapidly (figure 5*a*). The typical duration of these pulses is between 0.9 and 1.5 s but some of the data showed the existence of pulses longer than the duration of a linear camera exposure (3 s). In addition, under nearly identical conditions ($Ta = 7931$, $Re = 216$ and $e = 0.5\,\text{cm}$), we also noticed patches of upstream vortices with nearly the same high phase velocity (figure 5*b*). These pulses are more frequent beyond $Re = 350$. When the rotational speed increases, the duration of the pulses which appear during a linear camera exposure decreases and it is then difficult to distinguish them from localised defects like splitting or merging vortices. In the case of $e = 0.5\,\text{cm}$, the upstream patches occur more rarely than the downstream ones. The number of vortices forming these pulses is generally greater in this case. On the

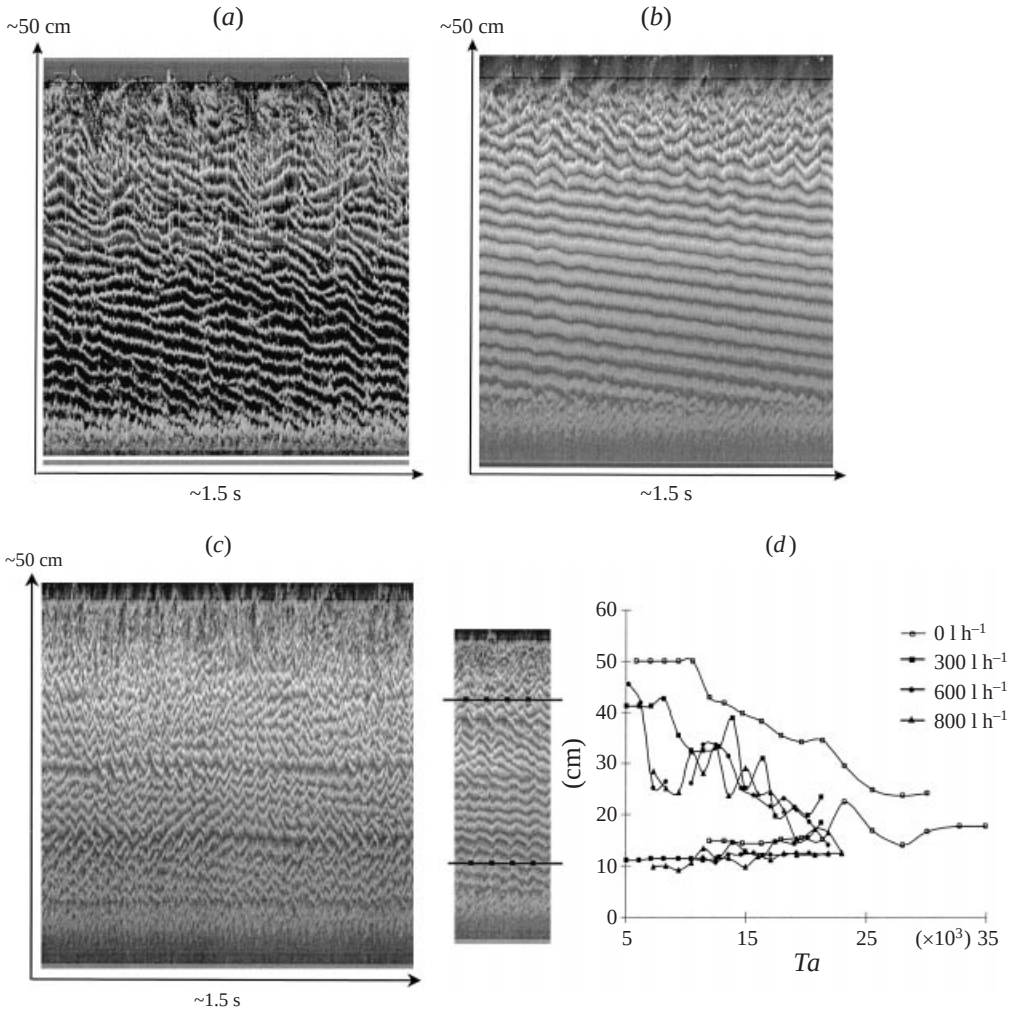

FIGURE 4. $e = 0.5$ cm. (*a*) At low Ta/Re ratios, merging and splitting of air bubble rings prevent steady parallel ring configuration (600 r.p.m., $Ta = 6555$; 700 l h^{-1}, $Re = 417$). (*b*) At higher Taylor numbers, parallel and independent rings can be seen being advected by the axial throughflow. Note that the amount of air entrained downward is more significant as the agitation of the top free surface increases. Air bubble sizes also decrease because of turbulent shearing (1200 r.p.m., $Ta = 12194$; 400 l h^{-1}, $Re = 221$). (*c*) At very high Taylor numbers, spatio-temporal defects dominate the flow, leading to the destruction of Taylor vortices (2200 r.p.m., $Ta = 25776$; 700 l h^{-1}, $Re = 191$). (*d*) Influence of the boundary conditions. The distance between lines of the same symbol is the effective length of the Couette–Taylor region where Taylor vortices can be clearly discriminated (see for example an image for $Re = 300$).

other hand, when $e = 1.0$ cm, the upstream patches are much more frequent than the downstream ones. The origins of these intermittent anomalous patches of patterns are not obvious. Nevertheless, we noticed that the inception of these spatial and temporal defects is generally preceded by high-amplitude fluctuations of the vortex boundaries.

The existence of these intermittent and random pulses of the full pattern modifies the existing conceptual scope of models for mass transfer, where the roll patterns are considered as series of constant numbers of chemical reactors.

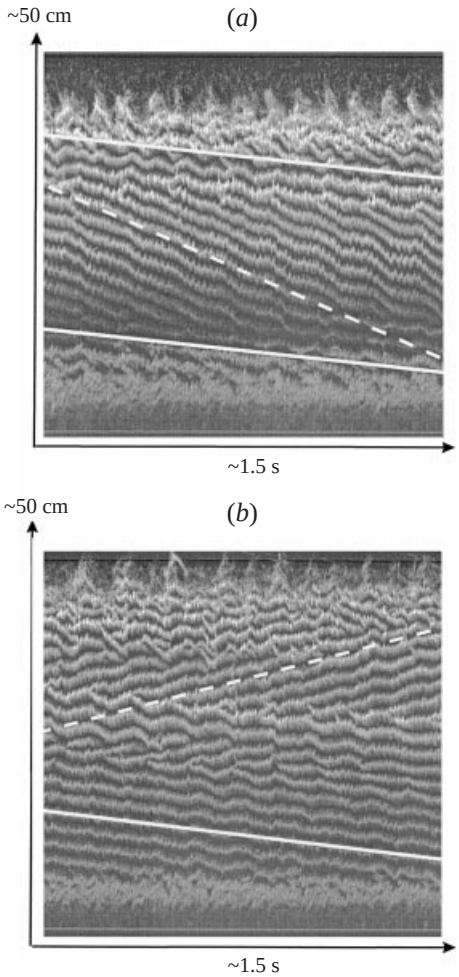

FIGURE 5. (*a*) Faster downstream waves (dashed line). This anomalous pulse of vortices travels with higher velocity than the mean axial wave propagation (solid line) ($e = 0.5$ cm, 700 r.p.m., $Ta = 6940$; 400 l h^{-1}, $Re = 216$). (*b*) Upstream waves (dashed line). Despite the fact that these operational conditions are very similar ($e = 0.5$ cm, 800 r.p.m., $Ta = 7931$; 400 l h^{-1}, $Re = 216$), the flow configurations are different.

3.2. *Flow pattern characteristics*

3.2.1. *Axial wavelength*

In the case of $e = 0.5$ cm we performed 180 measurements with Taylor numbers between 40 and 3.5×10^4 and axial Reynolds numbers between 0 and 560 using at the same time images and space/time diagrams obtained with the linear CCD camera. When $e = 1$ cm, the number of measurements was 168 with $Ta \in [40\,;\,10^5]$ and $Re \in [0\,;\,590]$.

We define the 'effective' wavelength of the Taylor cells as follows:

$$\lambda = \frac{\text{effective length of the Couette–Taylor region}}{\text{number of outflow boundaries}}$$

where the effective length of the Couette–Taylor region is presented in figure 4(*d*). This

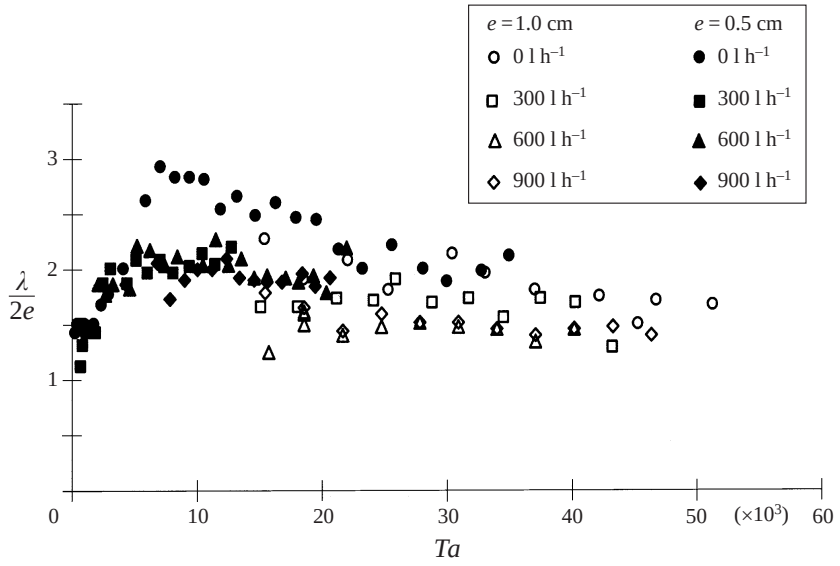

FIGURE 6. Axial wavelength of the vortices. λ is the height of a pair of vortices, e is the annular gap.

definition of the wavelength makes special provision for end effects or end boundary conditions. In practice, in most of the experiments, we can only count every other boundary (outflow boundaries) where air bubbles accumulate.

According to linear theory, just above the first bifurcation, the critical wavelength is $2e$. We observe a rapid increase in the axial wavelength when the Taylor number increases (figures 3*c* and 6). Without a throughflow, $\lambda/2e$ reaches its maximum value of 2.8 in the range of Taylor numbers from 5×10^3 to 10^4. High rotation speeds seem to stretch vortices vertically. Next, the value tends to decrease slowly to 1.7 at $Ta = 5.1 \times 10^4$. Spatial and temporal defects dominate the flow (above $Ta = 3.5 \times 10^4$ in the case of $e = 0.5$ cm and $Ta = 5.1 \times 10^4$ when $e = 1.0$ cm), inducing the destruction of the vortices.

With a superimposed axial flow, we observed the same trend despite the fact that the maximum values of λ did not exceed 2.3, whatever the value of the throughput from 300 to 900 l h^{-1}. Also, destruction of the vortices occurred sooner, above $Ta = 2.4 \times 10^4$ when $e = 0.5$ cm and $Ta = 4.6 \times 10^4$ when $e = 1.0$ cm. Therefore, an axial flow tends to squeeze cells vertically. As observed by Kaye & Elgar (1958) and Astill (1964), it also stabilizes the flow, as the first regular vortices appear later when the throughput increases.

Like Djéridi *et al.* (1998), in the vicinity of $Ta = 3 \times 10^3$ and without throughflow, we also noted a particular axial wavelength pattern consisting of one large vortex and one small one.

3.2.2. *Phase velocities*

The vortex axial displacement velocities were calculated by measuring slopes on space/time diagrams. For the mean dimensionless axial phase velocity V/V_m, we measured values around 0.9 regardless of the throughput (figure 7) in a wide region of the experimental parameters, which is less than the value of 1.1 to 1.2 usually found at lower Ta and Re and without a top free surface (Snyder 1962; Lueptow *et*

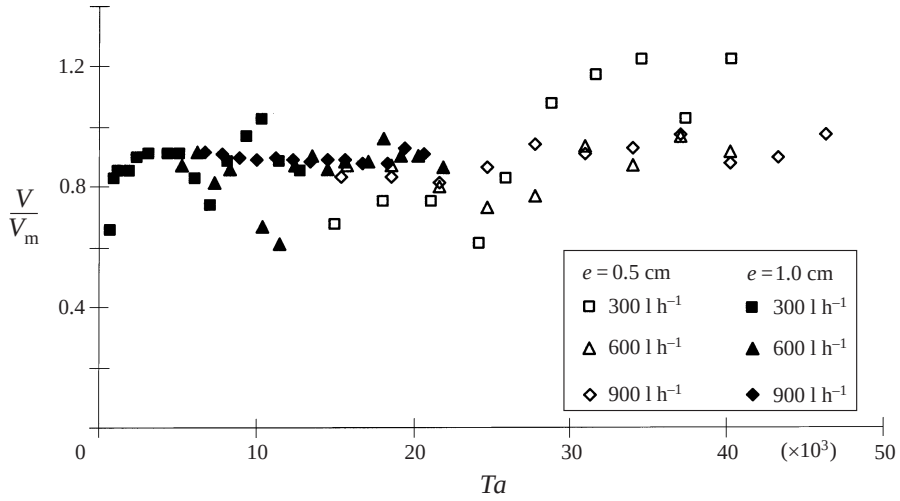

FIGURE 7. Axial phase velocities of the mean flow. V is the velocity of the axial displacement of the vortices, V_m is the mean axial velocity (ratio of throughput to gap cross-section).

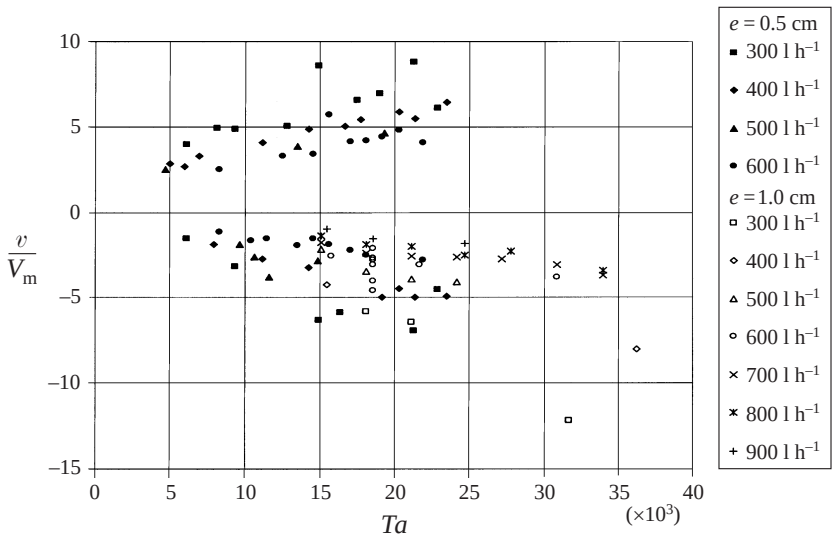

FIGURE 8. Axial phase velocities of the secondary axial waves. Positive values of v/V_m correspond to the faster downstream waves, while negative values are related to the upstream waves.

al. 1992; Piva *et al.* 1997; Wereley & Lueptow 1999). For higher Taylor and lower Reynolds numbers, we noticed an increase of V/V_m.

For the secondary axial wave propagation described above, we found much higher phase velocity values. In figure 8, we have indicated for several axial throughputs the dimensionless phase velocity of such waves v/V_m versus Taylor numbers from 5×10^3 to 3.6×10^4. We noticed first that the velocity of the downstream or upstream waves decreases with rising throughput. In addition, for a given throughput, we observed an increase in the phase velocity with the rotational speed. This increase tends to be less significant when the intensity of the throughput increases.

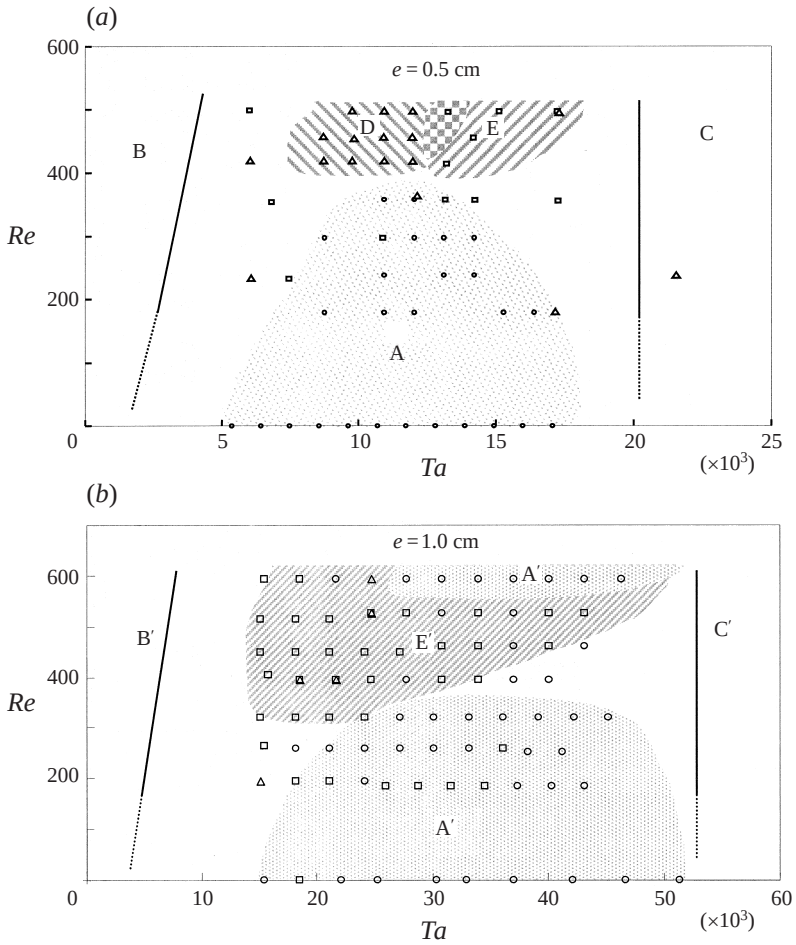

FIGURE 9. (*a*) Case of $e = 0.5\,\mathrm{cm}$: operating conditions where an ideal flow configuration can be expected (dots, region A). In region B, the Ta/Re ratio is too low and ordered patterns cannot be found. In region C, the gap is often invaded by defects (merging and splitting phenomena). For the downstream vortices travelling with high phase velocity, triangles indicate the experimental situations where pulses composed of 8 (or more) vortices appear. In region D, this phenomenon is particularly frequent. In the case of the upstream vortices, situations corresponding to pulses composed of 6 (or more) vortices are indicated with squares; they are more frequent in region E. (*b*) Case of $e = 1.0\,\mathrm{cm}$: corresponding regions described above are reported using the same letters (primed) and symbols.

4. Discussion and conclusion

According to these results, when $e = 0.5\,\mathrm{cm}$, the ideal flow configuration presented in figures 1(*a*) and 4(*b*) can be found in the region of the Taylor/Reynolds number map roughly defined by $Ta \in [10^4\,;\,1.7 \times 10^4]$ and $Re \in [0\,;\,400]$. In figure 9(*a*), the circles (region A) denote experimental situations without secondary patches (upstream or downstream pulses are very uncommon here). In the case of $e = 1.0\,\mathrm{cm}$, the corresponding ranges are defined by $Ta \in [1.6 \times 10^4\,;\,4.3 \times 10^4]$ and $Re \in [0\,;\,400]$ (region A′, figure 9*b*).

When the intensity of the throughflow is high compared with the rotational speed of the inner cylinder, the Taylor vortices are not fully developed. Thus, as reported

by other researchers (Gu & Fahidy 1985), the Ta/Re ratio is an accurate parameter defining the beginning of the 'ideal working zone' of such a chemical reactor. When Ta/Re is too low, we cannot find ordered patterns within the flows (see regions B and B′ in figure 9*a*, *b*).

However, when the Taylor number is too high, this ratio is no longer appropriate. In such conditions, the cell is often invaded by defects (figure 4*c*). In regions C ($Ta > 2 \times 10^4$) and C′ ($Ta > 5 \times 10^4$), the flow states correspond to experimental situations in which we can observe a considerable number of such defects. These particular patterns probably enhance the mixing between vortices because of splitting and merging phenomena related to the inception of these defects.

Considering the pulses of vortices travelling with high phase velocity, we noticed two different behaviours of the flow according to the size of the gap. In the case of $e = 0.5$ cm, we show with triangles the experimental situations where we found pulses composed of 8 (or more) downstream vortices. In region D of figure 9(*a*), this phenomenon is particularly frequent. In the case of the upstream vortices, situations corresponding to pulses composed of 6 (or more) vortices are indicated with squares; they are more frequent in region E. When $e = 1.0$ cm, the downstream vortices are particularly uncommon. Some of them were observed when $Ta \approx 2 \times 10^4$ and $Re \approx 400$. In the other hand, the patches of upstream vortices are widely observed in region E′ of figure 9(*b*).

This behaviour is like an absolute instability with upstream and downstream propagating fronts. Given a rotational velocity, the upper free surface is more agitated when the gap is smaller. In this case, the intense perturbation of the upper boundary favours the generation of downstream patches of vortices travelling with high phase velocity. When $e = 1.0$ cm, the influence of the free surface is less important and the upstream pulses are commonly observed. These upstream propagating patterns appear to be similar to the turbulent pulses observed by Deissler & Brand (1995). As these authors showed in numerical simulations of the quintic complex Ginzburg–Landau model for travelling patterns, the intrinsic dynamics related to the nonlinear coupling excite propagating localized states (pulses) capable of travelling in the upstream direction. This characteristic seems to be a general phenomenon but can be partially hidden by the influence of the boundary conditions (the agitation of the free surface in this case).

When $e = 1.0$ cm, on increasing the Taylor and Reynolds numbers (respectively $Ta \in [2.7 \times 10^4 ; 4.5 \times 10^4]$ and $Re \approx 590$) the high-speed linear camera exposures revealed another region where the ideal flow configuration is noticed. The intensity of the throughput and high velocities of the inner cylinder seem to prevent the development of upstream pulses and to favour classic travelling Taylor vortices.

For chemical engineering purposes (chemical reactor), a prototype working in regions A and A′ of the Taylor/Reynolds number map would allow good control of the residence time of chemical components within the flow. The Taylor vortices, corresponding to the well-mixed batch reactors, travel across the reactor with a dimensionless axial velocity close to 0.9. Compared with the 'ideal zone' described by Kataoka *et al.* (1975), this set of parameters ensures the correct dispersion of one liquid phase into the other one due to the intense shearing taking place in the gap. Moreover, previous work on this Couette device (Tison 1996) showed that under these conditions it was possible, from two immiscible liquids, to generate an emulsion composed of 200 μm diameter droplets.

In any event, the complexity of the turbulent spatial and temporal behaviour places a limitation on the classical consideration of this instability as an ideal mixing reactor,

and this first observation of the anomalous patches of travelling patterns modifies the previous simple view of the Couette–Taylor reactor.

In addition, work is in progress to study the dynamics of migration in a dispersed liquid–liquid system (aqueous and organic phases) in order to show the importance of the Laplacian operator of pressure in this transport mechanism (A. Babiano & O. Piro 1999, personal communication).

The first author (K.A.) was supported by a grant from the *Commissariat à l'Energie Atomique*. The authors would like to express their appreciation to Yann Viala and the PLATEC staff (CEA), for their helpful participation in the development of the experimental test bed and to Eric Magère and Michel O. Deville for the numerical computations.

REFERENCES

Astill, K. N. 1964 Studies of the developing flow between concentric cylinders with an inner rotating cylinder. *J. Heat Transfer* **86**, 383–391.

Bühler, K. & Polifke, N. 1990 Dynamical behaviour of Taylor vortices with superimposed axial flow. In *Nonlinear Evolution of Spatio-Temporal Structures in Dissipative Continuous Systems* (ed. F. H. Busse & L. Kramer), pp. 21–29. Plenum.

Davey, A., DiPrima, R. C. & Stuart, H. K. 1968 On the stability of Taylor vortices *J. Fluid Mech.* **31**, 17–52.

Deissler, R. J. & Brand, H. R. 1995 Interaction of breathing localized solutions for subcritical bifurcations. *Phys. Rev. Lett.* **74**, 4847.

Djéridi, H., Favé, J.-F., Billard, J. Y. & Fruman, D. H. 1998 Bubble capture and migration in Couette–Taylor flow. *Exps. Fluids* **26**, 233–239.

Favé, J.-F. 1999 Analyse des effets d'une phase disperseé par cavitation ou ventilation sur les structures de l'écoulement de Taylor–Couette. PhD thesis, Université de Nantes.

Gauthier, G., Gondret, P. & Rabaud, M. 1998 Motions of anisotropic particles: application to visualization of three-dimensional flows. *Phys. Fluids* **10**, 2147–2154.

Gu, Z. H. & Fahidy, T. Z. 1985 Characteristics of Taylor vortex structure in combined axial and rotating flow. *Can. J. Chem. Engng* **63**, 710–715.

Kataoka, K., Doi, M. & Hongo, N. 1975 Ideal plug-flow properties of Taylor vortex flow. *J. Chem. Engng Japan* **8**, 472–476.

Kataoka, K. & Takigawa, T. 1981 Intermixing over cell boundary between Taylor vortices. *AIChE J.* **27**, 504–508.

Kaye, J. & Elgar, E. C. 1958 Modes of adiabatic and diabatic fluid flow in an annulus with an inner rotating cylinder. *J. Heat Transfer* **80**, 753–763.

Landau, L. D. & Lifshitz, E. M. 1987 *Fluid Mechanics*, 2nd Edn. Pergamon.

Lathrop, D. P., Fineberg, J. & Swinney, H. L. 1992 Turbulent flow between concentric rotating cylinders at large Reynolds number. *Phys. Rev. Lett.* **68**, 1515–1518.

Ligrani, P. M., Longest, J. E., Kendall, M. R. & Fields, W. A. 1994 Splitting, merging and spanwise wavenumber selection of Dean vortex pairs. *Exps. Fluids* **18**, 41–58.

Lueptow, R. M., Docter, A. & Min, K. 1992 Stability of axial flow in an annulus with a rotating inner cylinder. *Phys. Fluids* A **4**, 2446–2455.

Magère, E., Deville M. O., Atkhen K. & Fontaine, J. 1998 Simulation of the pressure distribution in a spent nuclear fuel reprocessing Taylor–Couette device. In *Proc. Fourth ECCOMAS, Athens, Greece, September 7–11 1998*, Vol. 1, Part II, pp. 1094–1098. John Wiley and Sons.

Marcus, P. S. 1984 Simulation of Taylor–Couette flow. Part 2. Numerical results for wavy-vortex flow with one travelling wave *J. Fluid Mech.* **146**, 65–113.

Ohmura, N., Kataoka, K., Shibata, Y. & Makino, T. 1997 Intermixing over cell boundary between Taylor vortices. *AIChE J.* **27**, 504–508.

Piva, M., Calvo, A., Aguirre, A., Callegari, G., Gabbanelli, S., Rosen, M. & Wesfreid, J. E. 1997 Hydrodynamical dispersion in Taylor–Couette cells. *J. Phys. Paris* III **7**, 895–908.

Shiomi, Y., Kutsuna, H., Akagawa, K. & Ozawa, M. 1993 Two-phase flow in an annulus with a rotating inner cylinder (flow pattern in bubbly flow region). *Nucl. Engng Design* **141**, 27–34.

Snyder, H. A. 1962 Experiments on the stability of spiral flow at low axial Reynolds numbers. *Proc. R. Soc. Lond.* A **265**, 198–214.

Tam, W. & Swinney, H. L. 1987 Mass transport in turbulent Couette–Taylor flow. *Phys. Rev.* A **36**, 1374–1381.

Tison, E. 1996 Caractérisation de la zone de mélange d'un extracteur centrifuge à effet Couette utilisé en extraction liquide-liquide. PhD thesis, Institut National Polytechnique de Lorraine.

Treybal, R. E. 1981 *Mass Transfer Operations* McGraw-Hill, 3rd Edn.

Wereley, S. T. & Lueptow, R. M. 1999 Velocity field for Taylor–Couette flow with an axial flow. *Phys. Fluids* **11**, 3637–3649.